This figure "fig1.jpg" is available in "jpg" format from:

http://arXiv.org/ps/astro-ph/9806250v1

This figure "fig2pg1.jpg" is available in "jpg" format from:

http://arXiv.org/ps/astro-ph/9806250v1

 ${\bf TABLE~1}$ Density and Geometrical Parameters of the IPD Model

cloud component	parameter	description	final value	68% joint. conf. unc.
Smooth Cloud	n_0	density at 1 AU	$1.13 \times 10^{-7} \ \mathrm{AU^{-1}}$	6.4×10^{-10}
(Widened	α	radial power law exponent	1.34	0.022
Modified Fan)	β	vertical shape parameter	4.14	0.067
,	γ	vertical power law exponent	0.942	0.025
	μ	widening parameter	0.189	0.014
	i	inclination	2.03°	0.017
	Ω	asc. node	77.7°	0.6
	X_0	x offset from Sun	$.0119 \; \mathrm{AU}$	0.0011
	Y_0	y offset from Sun	$.00548 \; \mathrm{AU}$	0.00077
	Z_0	z offset from Sun	$00215 \; \mathrm{AU}$	0.00043
Dust Band 1	n_{B1}	density at 3 AU	$5.59 \times 10^{-10} \text{ AU}^{-1}$	7.20×10^{-11}
	$\delta_{\zeta_{B1}}$	shape parameter	8.78°	fixed
	v_{B1}	shape parameter	.10	fixed
	p_{B1}	shape parameter	4	fixed
	i_{B1}	inclination	0.56°	fixed
	Ω_{B1}	asc. node	80°	fixed
	$\delta_{R_{B1}}$	inner radial cutoff	$1.5~\mathrm{AU}$	fixed
Dust Band 2	n_{B2}	density at 3 AU	$1.99 \times 10^{-9} \text{ AU}^{-1}$	1.28×10^{-10}
	$\delta_{\zeta_{B2}}$	shape parameter	1.99°	fixed
	v_{B2}	shape parameter	.90	fixed
	p_{B2}	shape parameter	4	fixed
	i_{B2}	inclination	1.2°	fixed
	Ω_{B2}	asc. node	30.3°	fixed
	$\delta_{R_{B2}}$	inner radial cutoff	.94 AU	0.025
Dust Band 3	n_{B3}	density at 3 AU	$1.44 \times 10^{-10} \text{ AU}^{-1}$	2.34×10^{-11}
	$\delta_{\zeta_{B3}}$	shape parameter	15.0°	fixed
	v_{B3}	shape parameter	.05	fixed
	p_{B3}	shape parameter	4	fixed
	i_{B3}	inclination	0.8°	fixed
	Ω_{B3}	asc. node	80.0°	fixed
	$\delta_{R_{B3}}$	inner radial cutoff	1.5 AU	fixed
Solar Ring	n_{SR}	density at 1 AU	$1.83 \times 10^{-8} \text{ AU}^{-1}$	1.27×10^{-9}
	R_{SR}	radius of peak density	$1.03~\mathrm{AU}$	0.00016
	σ_{rSR}	radial dispersion	$0.025 \mathrm{\ AU}$	fixed
	σ_{zSR}	vertical dispersion	$0.054~\mathrm{AU}$	0.0066
	i_{RB}	inclination	0.49°	0.063
	Ω_{RB}	asc. node	22.3°	0.0014
Trailing Blob	n_{TB}	density at 1 AU	$1.9 \times 10^{-8} \text{ AU}^{-1}$	1.42×10^{-9}
	R_{TB}	radius of peak density	$1.06~\mathrm{AU}$	0.011
	σ_{rTB}	radial dispersion	0.10 AU	0.0097
	σ_{zTB}	vertical dispersion	$0.091~\mathrm{AU}$	0.013
	$ heta_{TB}$	longitude w.r.t. earth	-10°	fixed
	$\sigma_{ heta TB}$	longitude dispersion	12.1°	3.4

This figure "fig2pg2.jpg" is available in "jpg" format from:

http://arXiv.org/ps/astro-ph/9806250v1

The COBE Diffuse Infrared Background Experiment Search for the Cosmic Infrared Background: II. Model of the Interplanetary Dust Cloud

T. Kelsall, ^{1,2} J. L. Weiland, ³ B. A. Franz, ⁴ W. T. Reach, ⁵ R. G. Arendt, ³ E. Dwek, ¹ H. T. Freudenreich, ³ M. G. Hauser, ⁶ S. H. Moseley, ¹ N. P. Odegard, ³ R. F. Silverberg, ¹ and E. L. Wright ⁷

ABSTRACT

The *COBE* Diffuse Infrared Background Experiment (DIRBE) was designed to search for the cosmic infrared background (CIB) radiation. For an observer confined to the inner solar system, scattered light and thermal emission from the interplanetary dust (IPD) are major contributors to the diffuse sky brightness at most infrared wavelengths. Accurate removal of this zodiacal light foreground is a necessary step toward a direct measurement of the CIB.

The zodiacal light foreground contribution in each of the 10 DIRBE wavelength bands ranging from 1.25 to 240 μ m is distinguished by its apparent seasonal variation over the whole sky. This contribution has been extracted by fitting the brightness calculated from a parameterized physical model to the time variation of the all-sky DIRBE measurements over 10 months of liquid-He-cooled observations. The model brightness is evaluated as the integral along the line of sight of the product of a source function and a three-dimensional dust density distribution function. The dust density distribution is composed of multiple components: a smooth cloud, three asteroidal dust bands, and a circumsolar ring near 1 A.U. By using a directly measurable quantity which relates only to the IPD cloud, we exclude other contributors to the sky brightness from the IPD model.

¹Code 685, NASA GSFC, Greenbelt, MD 20771

²email: kelsall@stars.gsfc.nasa.gov

³Raytheon STX, Code 685, NASA GSFC, Greenbelt, MD 20771

⁴General Sciences Corp., Code 970.2, NASA GSFC, Greenbelt, MD 20771

⁵California Institute of Technology, IPAC/JPL, MS 100-22, Pasadena, CA 91125

⁶Space Telescope Science Institute, 3700 San Martin Drive, Baltimore, MD 21218

⁷UCLA Dept. of Astronomy, Los Angeles, CA 90024

Using the IPD model described here, high-quality maps of the infrared sky with the zodiacal foreground removed have been generated. Imperfections in the model reveal themselves as low-level systematic artifacts in the residual maps which correlate with components of the IPD. The most evident of these artifacts are located near the ecliptic plane in the mid-infrared, and are less than 2% of the zodiacal foreground brightness. Uncertainties associated with the model are discussed, including implications for the CIB search.

Subject headings: interplanetary medium — infrared: solar system—cosmology: observations — diffuse radiation — infrared: general

1. INTRODUCTION

The effort to understand the nature of the "zodiacal cloud" or interplanetary dust (IPD) cloud is of long standing. The first hypothesis for the cause of the zodiacal light was formulated over three centuries ago by Cassini (1685). He proposed on the basis of careful visual observations that the brightness pattern seen in the night sky could be caused by a lenticular cloud of dust centered on the Sun with its main axis lying in the ecliptic plane. This was an amazingly astute conclusion. Though much later in formulation, another insightful interpretation of the structure of the IPD cloud was forwarded by Fessenkov in the early 1940's (Struve 1943). Fessenkov considered the IPD distribution as a prolate spheroid surrounded by a dust torus formed from the fragmentation of the asteroids in the asteroid belt. Though even these early efforts came to reasonable conclusions as to the general shape of the IPD cloud, more recent data, such as those from the IRAS satellite and those from the COBE Diffuse Infrared Background Experiment (DIRBE), show the cloud structure to be rather more complex. The primary objective of the DIRBE, a search for the extragalactic infrared background, requires formulation of a detailed description of the IPD cloud so that its contribution to the sky brightness can be modelled and accurately removed from measurements of the diffuse sky brightness. The aim of this paper is to describe the model developed by the DIRBE team.

A wide variety of evidence indicates that within a few astronomical units (AU) of the Sun the solar system is filled with dust of cometary and asteroidal origin. The IPD reveals itself as a diffuse component of the sky brightness, attributed to the scattering of sunlight in the UV, optical and near-infrared, and the thermal re-radiation of absorbed energy in the midand far-infrared. At infrared wavelengths from approximately $1-100~\mu m$, the signal from the IPD is a major contributor to the diffuse sky brightness, and dominates the mid-infrared

 $(\sim 10-60 \ \mu \text{m})$ sky in nearly all directions except very low Galactic latitudes. With the aid of mid-infrared photometric measurements, our picture of the zodiacal cloud has evolved over the last fifteen years from a relatively simple smooth distribution of dust to one of increasing complexity. The terms "zodiacal cloud" and "IPD cloud" now encompass several distinct components, each of which may possess different grain properties and experience different orbital dynamics (Dermott et al. 1996; Leinert et al. 1998). In addition to a smooth background distribution arising from a mix of dust associated with asteroidal and cometary debris, there are also contributions from smaller scale structures. The IRAS data showed, and the DIRBE data confirm, that imposed on the brightness of the main cloud there are contributions from asteroidal dust bands (Low et al. 1984; Spiesman et al. 1995 and references therein). More recently, a circumsolar ring theoretically proposed to arise from dust spiralling in from the outer solar system and being resonantly trapped by the Earth in orbits near 1 AU (Gold 1975; Jackson and Zook 1989; Marzari and Vanzani 1994a, 1994b; Dermott et al. 1994) was compellingly confirmed by Reach et al. (1995) through use of a simple IPD model and the DIRBE data. Finer scale features such as dust trails in cometary orbits have also been observed in *IRAS* data (Sykes et al. 1986).

The issue as to the ultimate source of the dust is still open, but satellite observations of the sky brightness and in situ measurements of dust particles are advancing our understanding of the relative contributions from comets, asteroids, and the interstellar medium. From a study of 200 captured dust particles, Schramm, Brownlee, and Wheelock (1989) find that it is possible to ascribe 45% of the particles to cometary origin and 37% to asteroidal origin. Using dynamical analysis to construct the configuration of the IPD cloud from comets and asteroids, Liou, Dermott, and Xu (1995) found a match to the IRAS brightness profiles using a mixture of 74% cometary and 26% asteroidal dust. More recently, using numerical modelling to determine the evolution of dust from asteroidal collisions, Durda and Dermott (1997) find that 34% of the IPD could arise from collisional destruction of asteroidal family members (10%) and main-belt members (24%). In addition to the dust formed from members of the solar system, Baguhl et al. (1995) find in the Ulysses satellite dust-detection data a distinct signature in the impact directions indicating that interstellar dust is flowing into the solar system. The contribution to the brightness of the IPD from the interstellar dust is small, as shown by Grogan, Dermott, and Gustafson (1996), and it is not considered in the modelling described in this paper. Though there have been advances in estimating the source of the dust, reality appears to be yet more complex. Divine (1993) has shown from an interpretation of ground-based and satellite measurements that the IPD is best represented as being composed of five distinct dust-family components. On the basis of this work, Staubach, Divine & Grün (1993) have estimated the sky brightness arising from the five-component cloud. Clearly in the future there will be a strong symbiotic relationship between the modelling of the brightness of the IPD and the growing intricate and precise theoretical and observational studies of its nature.

Data from IRAS (Neugebauer et al. 1984; Beichman 1987) have been instrumental in advancing studies of the infrared zodiacal emission. However, the IRAS database does have some limitations, including relatively uncertain calibration of the photometric zero point, wavelength coverage only from 12 to 100 μ m, and sparse solar elongation sampling of most celestial directions. Diffuse infrared sky brightness measurements have been greatly extended by the Diffuse Infrared Background Experiment (DIRBE), launched as part of the Cosmic Background Explorer (COBE) in 1989. The DIRBE is an absolutely calibrated photometer with an instrumentally-established photometric zero point, designed to survey the sky in ten broad photometric bands from $1.25-240~\mu$ m. As described in more detail in § 2, the unique DIRBE scanning strategy and dense, continuous sampling of the sky at solar elongations from $64^{\circ}-124^{\circ}$ over a 10-month interval have provided a previously unequaled infrared photometric database from which to study the IPD in both scattering and thermal wavelength regimes.

A major thrust in photometric studies of the IPD is the construction of models which can be used to reproduce the observed brightness distribution. The development of such models is not always motivated by a wish to understand the IPD for itself, but rather as a means for removing an obfuscating foreground which masks contributions from Galactic and extragalactic sources. The focus of this paper is to describe the model for the IPD which has been used to remove the zodiacal foreground from each of the ten DIRBE bands to permit investigation of the residual sky brightness for evidence of the cosmic infrared background (CIB; defined here as all diffuse infrared radiation of extragalactic origin). Since it was anticipated that the CIB may be faint compared to the IPD and Galactic foregrounds, the aim has been to generate an IPD model which could reproduce the zodiacal brightness to within a few percent or better.

A number of models and modelling techniques have been developed to describe the infrared zodiacal light (e.g., Boulanger & Perault 1988; Jones & Rowan-Robinson 1993; Wheelock et al. 1994; Dermott et al. 1996). All models, including the one described here, have limitations brought about primarily because of the general lack of detailed information on IPD grain properties, populations, and spatial distribution. No previous modelling effort, however, has been designed to take advantage of the spectral, temporal and angular coverage which DIRBE provides.

The remainder of this paper describes the development of a parameterized physical model of the IPD in which the parameters are determined by requiring the model brightness to match the measured time-dependence of the sky brightness in fixed celestial directions over the whole sky. Section 2 briefly describes the DIRBE instrument, scan strategy, and data reduction methods. In § 3, the motivation behind the chosen modelling approach is discussed. The details of the model itself are presented in § 4. Results of the modelling, including uncertainties, are presented in § 5. Section 6 contains a discussion of the implications of the model uncertainties for the CIB search, and conclusions are presented in § 7.

This paper is part of a series outlining the analysis of DIRBE data in the search for the cosmic infrared background. Paper I (Hauser et al. 1998) reports the observational results of the DIRBE search, compares them with previous work, and briefly discusses their implications. The foreground removal techniques used in the DIRBE search are described in two separate papers: this paper (Paper II), and Paper III (Arendt et al. 1998), which describes the Galactic foreground removal procedures and summarizes the systematic uncertainties arising from the total foreground discrimination process. A further discussion of the cosmological implications of the results described in Paper I is presented by Dwek et al. (1998, Paper IV).

2. DIRBE INSTRUMENT AND DATA OVERVIEW

The data used in this analysis are broad-band photometric measurements obtained with the DIRBE instrument during its 10 months of cryogenic operation (1989 Dec 11 to 1990 Sep 21) aboard the Cosmic Background Explorer (COBE) satellite. A detailed description of the COBE mission has been given by Boggess et al. (1992), and the DIRBE instrument has been described by Silverberg et al. (1993). The DIRBE provided a simultaneous survey of the sky in 10 photometric bands at 1.25, 2.2, 3.5, 4.9, 12, 25, 60, 100, 140 and 240 μ m using a $0.7^{\circ} \times 0.7^{\circ}$ field of view. Linear polarization data were gathered in the three shortest wavelength bands, but those data are not used in the model described here.

A stable DIRBE photometric system was established using a combination of internal and celestial sources (COBE DIRBE Explanatory Supplement 1997). The short-term instrumental gain stability, during the ten months of cryogenic operation at 1.8 K, was maintained using observations of a stable internal stimulator \sim 6 times per orbit. The long-term gain stability was monitored using bright stable celestial sources observed during normal sky scans, which were placed on an instrument-unique relative photometric system. The combination of using both the internal stimulators and celestial sources achieved a relative photometric system that was stable to $\sim 1\%$ over the cryogenic mission at most wavelengths.

The data at 100 μ m, however, had a special photometric problem. The Ge:Ga detector used at these wavelengths exhibited a gain instability referred to as "photon induced

responsivity enhancement" (PIRE; COBE DIRBE Explanatory Supplement 1997). PIRE effect is a form of hysteresis evidenced by an increase in responsivity when the DIRBE beam swept across a bright extended region, such as the inner Galaxy and the Cygnus spiral arm. The brightness recorded in pixels in the vicinity of these regions depended on the direction from which they were approached (i.e., on the brightness of the pixels previously scanned), with differences at 100 μ m as large as 25%. A non-linear correction was developed to mitigate the PIRE effect on the data. This correction significantly reduced the effect, leaving residual scan-dependent differences of the order of 5% or less, though in the brightest Galactic regions differences can still be as large as 10%. In contrast, the Ge:Ga detector used at 60 μ m, for which a PIRE correction was not implemented, was better-behaved, registering a difference of no more than 3%. Since the direction from which each pixel was approached in the survey varied in a systematic way with time, the PIRE effect may have created a spurious apparent temporal modulation of the brightness. Such modulation would not be coherent over a span of more than a few degrees, and would occur only at low Galactic latitudes. Since our search for the CIB excluded regions at low Galactic latitude (Paper I), this does not pose a serious problem for the DIRBE investigation.

Another essential feature of the calibration was the monitoring of the shape and centroids of the beams for each detector. This was done by assembling the transit data from selected bright celestial sources. The location of any transit was determined to the order of 1.5 arcminutes, which is a very small fraction of the 42-arcmin DIRBE beam. We found no solid angle variations in any band during the 10 months of cryogenic operation. Any variation must be smaller than the accuracy with which we were able to measure the solid angle, which was better than 1% from 1.25 to 25 μ m, and better than 5% from 60 to 240 μ m. These numbers include the uncertainty due to the possible contribution of stray light. The month-to-month beam centroid peak-to-peak variations during the cold mission were at most 1 arcminute. Errors in the centroid correction for wavelengths from 1.25 to 4.9 μ m are certainly much less than this because the reference beams for these bands were formed during intervals in which the variation about the mean was much less than 1 arcminute. Beam centroid errors for the longer wavelength bands, for which a single reference beam was used for the entire cold mission, are estimated to be less than 0.5 arcminute.

The absolute gain calibration at each wavelength was based upon observations of a single well-calibrated celestial object. The selected calibration objects were Sirius (1.25–12 μ m), NGC 7027 (25 μ m), Uranus (60 and 100 μ m), and Jupiter (140 and 240 μ m). The uncertainty in the absolute gain calibration is $\sim 3-5\%$ at 1.25 – 12 μ m and $\sim 10-15\%$ at 25 – 240 μ m (Paper I). The DIRBE intensity measurements are reported in units of MJy sr⁻¹, quoted at the ten nominal wavelengths with effective bandwidths calculated assuming the observed source energy distribution is $\nu I_{\nu} = \text{constant}$. This necessitates the use of a color correction

when computing the zodiacal light contribution ($\S 4$).

A critically important part of the DIRBE calibration, and one which distinguishes the DIRBE from most other infrared instruments, was establishing a true zero point for the photometric system. This was accomplished instrumentally. The DIRBE optical system was a totally off-axis design with multiple field and pupil stops which limited external stray light to levels well-below the sensitivity limit for the measurements at all wavelengths, $\nu I_{\nu} < 1 \text{ nW m}^{-2} \text{ sr}^{-1}$. The DIRBE instrument was equipped with a cold chopper, which modulated the beam at 32 Hz, and a cold shutter located at a field stop which could completely shut out sky light from reaching the detectors. When the shutter was open, each detector measured the difference between the sky brightness and that of an internal beam stop maintained at a temperature below 3 K so as to emit essentially no flux at the DIRBE wavelengths. The shutter was closed about six times per orbit and the instrumental offset signal at 32 Hz was measured. This offset was stable throughout the entire 10 month cryogenic mission, and was subtracted from the data obtained while scanning the sky. A real radiative instrumental offset was present, largely due to emission from the JFETs used in the signal amplifiers for the detectors which were mounted in the detector assemblies. This offset, which was significant only at wavelengths of 60 μ m and longer, was confirmed by turning off the JFETs sequentially and measuring the change in offset in the other detectors. The offset uncertainty was carefully assessed using special on-orbit tests, which showed that the size of the offset did not depend on whether the shutter was open or closed. The zeropoint uncertainty, which is substantially below the sky brightness at all wavelengths, does not affect the IPD model, but does affect the systematic uncertainty in the CIB at long wavelengths (Paper I).

The observing strategy for DIRBE was designed to monitor the change in the sky brightness contribution from the IPD toward each celestial line of sight as a function of time, thus providing a richer infrared database for studying the IPD cloud than previously available. Like IRAS, the COBE spacecraft was placed in a Sun-synchronous polar orbit at 900 km altitude, but, unlike IRAS, the spacecraft also rotated (rate ~ 0.8 rpm). The COBE spin axis was nominally held fixed at an angle of 94° from the Sun, with the DIRBE instrument line-of-sight angled 30° from the spin axis. The 30° cant caused the DIRBE to execute a cycloidal track on the sky as the COBE both rotated and orbited the Earth. With a half-angle of 30°, the viewing swath enclosing this track covered one half of the sky after one orbit of the spacecraft (Fig. 1a). Because the field-of-view of the DIRBE was $0.7^{\circ} \times 0.7^{\circ}$, and the COBE orbital velocity was about 3.5° /minute, the one-orbit scan swath had gaps in coverage. Full sampling of one-half of the sky was achieved after about 1 day of observations (Fig 1b); the highest density of observations occurred along the edges of the viewing swath, and the lowest density at the center of the swath. It also follows from the scanning geometry

that the solar elongation angle (angle between the Sun and the line-of-sight) at which an observation was made is dependent on the location within the viewing swath: those positions along the swath edges closest to the Sun were viewed at elongations $e \sim 64^{\circ}$, and those along the edges furthest from the Sun at $e \sim 124^{\circ}$, with a smooth continuum between.

The COBE orbit precessed one degree per day, so the DIRBE viewing pattern on the sky shifted by this amount along the ecliptic plane each day. Complete sky coverage was thus achieved within four months, with more uniform sampling in six months. Figures 1c and 1d show the average of all observations of the sky at 12 μ m for periods of one week and the full mission, respectively. Because of the 1°/day orbital precession, a fixed celestial location near the ecliptic plane was observed at solar elongations from 64° to 124° over the course of 60 days each half year. Above ecliptic latitudes of $\sim 60^{\circ}$ the amplitude of the full range in elongation decreases about two degrees per degree of latitude, and is zero directly at the ecliptic poles. In this way, all accessible solar elongation angles in the range 64° to 124° were sampled for each location on the sky.

The photometric data from the DIRBE time-ordered scans described above were converted into maps of the sky by associating each observation with a pixel in the quadrilateralized spherical cube projection (O'Neill & Laubscher 1976; COBE DIRBE Explanatory Supplement 1997) in geocentric ecliptic coordinates, epoch 2000. The map resolution was chosen such that pixels are roughly 0.32° on a side, yielding 393,216 approximately equal-area pixels. A set of forty-one Weekly Sky Maps was created for the period of cryogenic operation, in which all individual observations of pixels sampled during one week were robustly averaged to produce a single average intensity per pixel at each wavelength. Pixels within $\sim 60^\circ$ of the ecliptic plane typically have $\sim 10-15$ samples per week over which to average; the most densely sampled pixels near ecliptic latitudes $|\beta|=60^\circ$ have ~ 30 samples per week. The averaging interval of one week was chosen so as not to overly smear apparent temporal variations of the zodiacal light (compare Figs. 1b and 1c), and yet provide a reasonably compact database. This set of Weekly Sky Maps is the basis for this study; specifically the Pass 3b version of these products released through the NSSDC in 1997.

All analysis has been performed using data from the original sky-cube coordinate system. For illustrational purposes, maps shown in this paper are reprojected into an ecliptic coordinate Mollweide projection. The Mollweide projection is an equal-area projection with the convenient properties that longitudes are equally spaced at each latitude and all lines of constant latitude are straight horizontal lines (though unequally spaced).

3. MOTIVATION AND MODELLING TECHNIQUE

The development of the IPD cloud model was driven by requirements imposed by the ultimate goal of determining the contribution of the isotropic CIB signal in the infrared. Thus, the method described here was designed to provide a means for accurately subtracting the zodiacal signal from the DIRBE observations at 1.25 through 240 μ m, while preserving any isotropic component of the sky brightness unrelated to the IPD; i.e., our method includes no arbitrary zero-point constants. The scheme follows what is now a canonical approach adopted in early models (Haug 1958; Leinert et al. 1976) of representing the IPD cloud geometric and radiative characteristics in a parametric form. This procedure has been utilized in a number of recent investigations (e.g., Murdock & Price 1985; Deul & Wolstencroft 1988; Rowan-Robinson et al. 1990; Jones and Rowan-Robinson 1993). The physics of the IPD cloud is embedded in the representations of the scattering and emissivity functions and the form factors for the various components (i.e., main cloud, asteroidal bands, and circumsolar ring).

Figures 2a and 8a illustrate the nature of the difficulty in generating such a model. The observed infrared sky brightness is a complex mix of foregrounds due to interplanetary dust, starlight, and interstellar dust, as well as an extragalactic background which is presumed to be isotropic. The relative mixture of foregrounds is wavelength dependent; only in the mid-infrared does emission from the IPD contribute 90% or more of the total sky brightness. Although the shape of the underlying zodiacal "lower envelope" is clearly visible in the figures from $1.25-100~\mu m$, spatially disentangling the Galaxy from the IPD signal with high precision is challenging (Hauser 1988). The problem is additionally complicated by the presence of low-constrast, smaller scale structures within the IPD cloud such as the dust bands and circumsolar ring (§ 4.2.2 and § 4.2.3).

In order to determine the contribution from interplanetary dust without modifying any of the other contributions, the one unique signature of the zodiacal light is used: it is the only component of the sky brightness that is not fixed on the celestial sphere. For an Earth-based observer, the IPD brightness observed in a given celestial direction on a given day depends on the observer's viewing aspect. Changes in viewing aspect resulting from the DIRBE cycloidal scan strategy and motion through the IPD cloud cause different path lengths through the dust to be sampled (and thus different portions of the dust density and temperature distributions), which gives rise to apparent temporal variations in the brightness observed toward a fixed celestial direction. Figure 3 is a schematic representation of how the zodiacal cloud signal is modulated in two directions. Toward the ecliptic pole (Fig. 3a), the main causes for variation of the brightness are the motion of the Earth with respect to the inclined midplane of the dust distribution, as well as the motion of the Earth radially due

to its orbital eccentricity. At lower latitudes (Fig. 3b), the apparent temporal variation is primarily due to the changing solar elongation of the line of sight as the Earth orbits about the Sun.

The technique used here exploits these effects to separate the light scattered and emitted by the IPD from all other brightness contributions by imposing an analytical form for the interplanetary dust density distribution, thermal emission characteristics, and scattering phase function. This parameterized model is then optimized to match the observed temporal variations in selected directions. The formulation of the parameterized model is described in § 4. Once the best-fit model parameters are determined, the brightness of the zodiacal light is then evaluated for all DIRBE weekly observations via a line-of-sight integral of the three-dimensional model.

4. PARAMETRIC IPD MODEL

The DIRBE IPD model is a parameterized physical model whose formulation is similar, but not identical, to that used in creating the *IRAS* Sky Survey Atlas (Wheelock et al. 1994). The DIRBE model consists of the integral along the line of sight of the product of a source function and a three-dimensional density distribution function. The emissivity function includes both thermal emission and scattering terms. The 3-dimensional dust density distribution is composed of multiple components – a smooth cloud, three dust bands, and a circumsolar dust ring just beyond 1 AU. Earlier versions of the model have been described by Reach et al. (1996) and Franz et al. (1996).

4.1. The Brightness Integral

The model for the IPD foreground computes the brightness of the zodiacal light observed at wavelength λ for each pixel p at time t as the integral along the line-of-sight of scattered and thermal emission contributions, summed over each density component c:

$$Z_{\lambda}(p,t) = \sum_{c} \int n_{c}(X,Y,Z) [A_{c,\lambda}F_{\lambda}^{\odot}\Phi_{\lambda}(\Theta) + (1 - A_{c,\lambda})E_{c,\lambda}B_{\lambda}(T)K_{\lambda}(T)] ds, \qquad (1)$$

where $n_c(X, Y, Z)$ is the three-dimensional density for each of the components, $A_{c,\lambda}$ is the albedo for component c at wavelength λ , F_{λ}^{\odot} is the solar flux, $\Phi_{\lambda}(\Theta)$ is the phase function at scattering angle Θ , $E_{c,\lambda}$ is an emissivity modification factor, which measures deviations from the blackbody thermal radiance function $B_{\lambda}(T)$, and $K_{\lambda}(T)$ is the DIRBE color-correction factor appropriate for $B_{\lambda}(T)$. The dust grain temperature T is assumed to vary with distance

from the Sun as $T(R) = T_0 R^{-\delta}$. The derived model value of $\delta = 0.467$ is very close to the theoretical value of 0.5 for large grey grains in radiative equilibrium.

As in the case of IRAS photometry, the DIRBE broad-band photometric measurements I_{λ} are quoted at fixed nominal wavelengths with bandwidths determined assuming the source energy distribution is $\lambda I_{\lambda} = \text{constant}$. Since the model parameters are optimized by fitting to the DIRBE data, a color correction $K_{\lambda}(T)$ must be applied to each evaluation of the blackbody source term in order to compute the zodiacal brightness in a fashion consistent with the DIRBE database; this is equivalent to convolving the source function with the DIRBE spectral response. A color-correction of 1.0 is used for the scattering source function. The color corrections are taken from those tabulated in the COBE DIRBE Explanatory Supplement (1997).

The treatment of the albedos $A_{c,\lambda}$ and emissivity modification factors $E_{c,\lambda}$ is important for this work. The aim is to achieve high accuracy in modelling the zodiacal light from $1.25-240 \mu m$, but the accuracy of the absolute calibration from wavelength to wavelength in the mid-infrared is relatively poor (§ 2). Furthermore, it is unlikely that the assumption of a single grain temperature at each distance R is entirely accurate. Models for the emission from interplanetary dust predict that a small range of temperatures contributes to the mid-infrared emission, expanding to a wider range at shorter wavelengths (Reach 1988). The wavelengthdependence of the albedo is essentially unknown, and a constant albedo is unlikely. In order to allow for the imprecision of the band-to-band calibration as well as the restrictive nature of the spectral model, the factors $A_{c,\lambda}$ and $E_{c,\lambda}$ are allowed to be free parameters. Albedos are allowed to be non-zero only at the shorter wavelengths (1.25, 2.2, & 3.5 μ m) and $E_{c,\lambda}$ is set to 1.0 at 1.25 and 2.2 μ m. The $E_{c,\lambda}$ is normalized to unity at 25 μ m. As coded, each density component could have its own particle properties, as delineated by $A_{c,\lambda}$ and $E_{c,\lambda}$. In practice, however, we allowed for three groups of $A_{c,\lambda}$ and $E_{c,\lambda}$: one for the smooth cloud, one for all of the dust bands, and one for the circumsolar ring. In addition, at $1.25-3.5 \mu m$, where the dust bands and circumsolar ring have a small contribution to the cloud brightness, the ring and dust band values for $A_{c,\lambda}$ and $E_{c,\lambda}$ were not optimized, but rather assumed to be identical to the values found for the smooth cloud at those wavelengths.

There is no definitive work which establishes a phase function in the infrared. Initial modelling attempts used the Henyey-Greenstein formulation determined by Hong (1985) for visible data, which allowed for no dependence of the phase function on wavelength. The final model incorporated a wavelength-dependent three-parameter functional form which was capable of reproducing the shape of Hong's function, but could also be optimized for the infrared. The functional form of the phase function $\Phi_{\lambda}(\Theta)$ is

$$\Phi_{\lambda}(\Theta) = N \left[C_{0,\lambda} + C_{1,\lambda}\Theta + e^{C_{2,\lambda}\Theta} \right]$$
 (2)

where Θ is the scattering angle in radians. The three free parameters for each wavelength are C_0 , C_1 and C_2 . The factor N is not free, being a function of the three C parameters and serving to normalize the phase function such that the integral over 4π steradians is 1.

4.2. Model Components and Geometry

The model calculations are performed in heliocentric ecliptic coordinates, (X, Y, Z). The coordinate transformation for a grid point at a distance s from the Earth along a line-of-sight at geocentric ecliptic coordinates (λ, β) is

$$X = R_{\oplus} \cos \lambda_{\oplus} + s \cos \beta \cos \lambda$$

$$Y = R_{\oplus} \sin \lambda_{\oplus} + s \cos \beta \sin \lambda$$

$$Z = s \sin \beta$$

$$R = \sqrt{X^2 + Y^2 + Z^2}$$
(3)

where R_{\oplus} is the Earth–Sun distance, and λ_{\oplus} is the heliocentric longitude of the Earth $(\lambda_{\oplus} = \pi - \lambda_{\odot})$ on the date of observation. The eccentricity of the Earth's orbit was included in the model.

The integration along the line of sight was performed by Gauss-Laguerre quadrature with 50 points. For ecliptic latitudes $|\beta| \leq 20^{\circ}$, Simpson's rule with ~ 200 steps was used in order to more accurately evaluate density gradients in small-scale structures closer to the ecliptic plane. Integration along the line of sight is performed from the Earth to an outer radial cutoff of 5.2 AU from the Sun, which roughly corresponds to the orbit of Jupiter.

All dust density components were assumed to be intrinsically time-independent and to have a plane of symmetry (although not necessarily the same plane in all cases). The only exception to this is the trailing blob in the circumsolar ring, which follows the Earth in its orbit. Isodensity contours of the total model density and its components are shown in Figure 4. The parameterized form used for each of these components is described in detail below.

The center of the smooth dust cloud was allowed to be offset from the Sun by (X_0, Y_0, Z_0) , so that the cloud coordinates were translated as follows:

$$X' = X - X_0$$

$$Y' = X - Y_0$$
 (4)
 $Z' = Z - Z_0$
 $R_c = \sqrt{X'^2 + Y'^2 + Z'^2}$.

The symmetry plane of the smooth cloud was also allowed to be tilted with respect to the ecliptic plane, so that the vertical structure is dictated by the height above the tilted midplane:

$$Z_c = X' \sin \Omega \sin i - Y' \cos \Omega \sin i + Z' \cos i, \tag{5}$$

where i and Ω are the inclination and ascending node of the midplane, respectively.

The density of the smooth cloud was presumed to be of a form which is separable into radial and vertical terms:

$$n_c(X, Y, Z) = n_0 R_c^{-\alpha} f(\zeta), \tag{6}$$

where $\zeta \equiv |Z_c/R_c|$. The separation into radial and vertical terms is typical of several models for the cloud density in the literature (e.g., as summarized by Giese et al. 1986). However, it should be noted that there are some theoretical reservations as to its applicability to modelling the IPD cloud (Banaskiewicz, Fahr and Scherer 1994; Fahr, Scherer and Banaskiewicz 1995). The radial power-law is motivated by the radial distribution expected for particles under the influence of Poynting-Robertson drag, which causes their orbital semi-major axes to decay such that their equilibrium distribution is 1/R. The assumption that the vertical distribution depends only on ζ is motivated by the fact that Poynting-Robertson drag does not affect the orbital inclination of particles as they spiral into the Sun. The radial power-law index, α , is a free parameter.

The vertical distribution $f(\zeta)$ was written in a form respresenting a widened, modified fan model:

$$f(\zeta) = e^{-\beta g^{\gamma}},\tag{7}$$

where

$$g = \begin{cases} \zeta^2/2\mu & \text{for } \zeta < \mu \\ \zeta - \mu/2 & \text{for } \zeta \ge \mu \end{cases}$$

and β , γ and μ are free parameters. (Note that β is not to be confused with the geocentric ecliptic latitude.) The vertical distribution is critically important in connecting the local density of the dust, which is very well determined by the DIRBE data, with the integrated column density.

This model is somewhat different from the one fitted to the IRAS data in production of the IRAS Sky Survey Atlas (Wheelock et al. 1994), because we used a spherical radius rather than a cylindrical one. Furthermore, the function g, which replaces ζ in the exponential of

the IRAS model, rolls off at small values and avoids the cusp in the midplane that is present in traditional fan models. Isodensity contours of the smooth cloud model are shown in Figure 4b.

4.2.2. Dust Bands

The dust bands were discovered in the IRAS data (Low et al. 1984), and are believed to be asteroidal collisional debris (Dermott et al. 1984; Sykes et al. 1989). The dust bands have been studied using the DIRBE data (Spiesman et al. 1995), confirming the observational results from IRAS data and extending them to the near-infrared. In particular, the parallactic and spectroscopic distances to the bands are less than the distance to the asteroid belt, so that the material producing them is likely to be debris spiralling into the Sun under Poynting-Robertson drag. Three band pairs are included, which appear at ecliptic latitudes around $\pm 1.4^{\circ}$, $\pm 10^{\circ}$ and $\pm 15^{\circ}$ in the sky maps. These have been attributed (Sykes et al. 1989, Reach et al. 1997) to a blend of the Themis and Koronis families ($\pm 1.4^{\circ}$), the Eos asteroid family ($\pm 10^{\circ}$), and the Maria/Io family ($\pm 15^{\circ}$). All band pairs were centered on the Sun, but were allowed to be inclined with respect to the ecliptic plane. Each band pair i had its own inclination i_{Bi} and ascending node Ω_{Bi} . A transformation similar to that in equation 5 was used to define the vertical distance from the midplane of band pair i, z_{Bi} .

For this work, a dust band density based on the migrating model (Reach 1992) was used, but with a simpler analytic formulation that is easier to evaluate and optimize. A modification was added in the form of a multiplicative factor which allowed for only "partial" migration, i.e., a cut-off at a minimum radius:

$$n_{Bi}(X,Y,Z) = \frac{3n_{3Bi}}{R} \exp\left[-\left(\frac{\zeta_{Bi}}{\delta_{\zeta_{Bi}}}\right)^{6}\right] \left[v_{Bi} + \left(\frac{\zeta_{Bi}}{\delta_{\zeta_{Bi}}}\right)^{p_{Bi}}\right] \left\{1 - \exp\left[-\left(\frac{R}{\delta_{R_{Bi}}}\right)^{20}\right]\right\}, \quad (8)$$

where n_{3Bi} is the density at 3 AU of band i, $\zeta_{Bi} \equiv |z_{Bi}/R_c|$, and $\delta_{\zeta_{Bi}}, v_{Bi}$ and p_{Bi} are adjustable shape parameters. The parameter $\delta_{R_{Bi}}$ determines the distance to which band i migrates in toward the Sun.

4.2.3. Circumsolar Ring

The Earth temporarily traps migrating dust particles into resonant orbits near 1 AU if they are in low-eccentricity orbits, as is expected for asteroidal debris (Jackson and Zook 1989; Marzari and Vanzani 1994a, 1994b; Dermott et al. 1994; Dermott 1996). We have

confirmed the existence of the dust ring near 1 AU by subtracting a smooth cloud model from two weekly sky maps, revealing the signature of the ring in remarkable agreement with the predictions (Reach et al. 1995). For the DIRBE IPD model, an empirical ring density function was developed to emulate the numerical simulations of Dermott et al. (1994). It consists of a circular toroid with an enhancement in a 3-dimensional blob trailing the Earth. This representation ignores the fact that the trailing blob follows the Earth in an equally eccentric orbit. Neglect of this effect is expected to introduce only a small error, though it will affect a large range in ecliptic latitude. This effect may be worth consideration in future models. As with the smooth cloud and dust bands, the symmetry plane of the ring complex (ring + trailing blob) was allowed to be inclined with respect to the ecliptic plane; the vertical distance above the ring midplane is denoted by Z_R , and is computed using equation 5, with the optimized values of Ω_{RB} and I_{RB} . The three-dimensional ring dust density distribution is modelled as

$$n_{R}(X, Y, Z) = n_{SR} \exp \left[-\frac{(R - R_{SR})^{2}}{2\sigma_{rSR}^{2}} - \frac{|Z_{R}|}{\sigma_{zSR}} \right]$$

$$+ n_{TB} \exp \left[-\frac{(R - R_{TB})^{2}}{2\sigma_{rTB}^{2}} - \frac{|Z_{R}|}{\sigma_{zTB}} - \frac{(\theta - \theta_{TB})^{2}}{2\sigma_{\theta TB}^{2}} \right]$$
(9)

where the subscript "SR" stand for the circumsolar ring and "TB" stands for the trailing blob. The σ values are free parameters for scale lengths in the R, Z_R and θ coordinates. Also free are the radial locations of the peak density of the ring (R_{SR}) and blob (R_{TB}) and the peak densities n_{SR} and n_{TB} .

The angle θ is the heliocentric ecliptic longitude relative to the mean longitude of the Earth. We have presumed that the ring structure is fixed with respect to the mean longitude of the Earth and not its true longitude. In these coordinates, the Earth moves in an epicycle about its mean longitude with an amplitude of 2°. The location of the trailing enhancement is $\theta_{TB} \sim 10^{\circ}$, so the epicyclic motion of the Earth changes its distance from the enhancement by $\sim 10 - 20\%$ over the year. Isodensity contours of the dust ring model are shown in Figure 4d. The map in Figure 4d cuts through the ring at 1 AU in two places, yielding the two cross-sectional slices. Note that the orientation of the map is rotated about the Z axis by θ_{TB} so that it cuts through the trailing blob.

4.3. Fitting Technique

The parameters of the IPD model are determined using the Levenberg-Marquardt non-linear least-squares optimization algorithm (Bevington 1969). The fit is constrained using only the observed time variation along independent lines-of-sight, while ignoring their

underlying photometric baselines. This is achieved by forcing the mean of the model over all time samples to match the mean of the data for each individual line-of-sight. In this way, the optimization procedure only has enough information to match the amplitude and phase of the temporal variation for each line-of-sight, with no assumption about the morphology or spectrum of non-varying components. The goodness of fit is defined so that the model is optimized to match the modulation as follows. Let t be the observation time (an index over the weekly sky maps), p be the celestial position (an index over selected pixels), and λ be the wavelength (an index over spectral bands). The observed brightness is $I_{\lambda}(p,t)$, and the model evaluated for the same conditions is $Z_{\lambda}(p,t)$. Then the goodness of fit is defined as

$$\chi^2 = \sum_{\lambda, p, t} \frac{1}{\sigma_{\lambda}^2(p, t)} \{ [I_{\lambda}(p, t) - \langle I_{\lambda}(p, t) \rangle_t] - [Z_{\lambda}(p, t) - \langle Z_{\lambda}(p, t) \rangle_t] \}^2.$$
 (10)

In this equation, $\sigma_{\lambda}^2(p,t)$ is the estimated uncertainty on $I_{\lambda}(p,t)$, as derived from the quadrature sum of random measurement errors and the uncertainty in the temporal stability of the gain calibration. A typical value for σ_{λ} in the 1.25 – 4.9 μ m bands is .005 MJy/sr. The 12 – 100 μ m sigma values are dominated by the temporal gain calibration uncertainty: typical values are best expressed in terms of $\frac{\sigma_{\lambda}}{I_{\lambda}}$, and are \sim .0076, .0076, .015 and .022, respectively. The 140 and 240 μ m bands, which are dominated by instrumental noise, have typical sigmas of 7 and 4 MJy/sr.

The parameters T_0 , $A_{c,\lambda}$ and $E_{c,\lambda}$ are highly correlated with each other, and cannot be determined independently. The value of T_0 was determined by running a preliminary fit which assumed that the smooth cloud is the dominant component and that the spectrum in the mid-IR is that of a pure blackbody; i.e., the albedos and emissivities at 4.9, 12 and 25 μ m were set to $A_{\lambda} = 0$ and $E_{\lambda} = 1.0$, and the model solved for T_0 . This value of T_0 was then fixed and subsequently used in all further fits for geometry and source terms.

Initially, the complete set of model parameters (geometry and source terms) were determined simultaneously using data from all 10 DIRBE wavelength bands. In order to avoid excessive computational requirements, the fitting dataset was chosen from a subset of the 41 weekly-averaged DIRBE maps. A spatial grid was established for each wavelength which sampled a sky pixel every $\sim 5^{\circ}$ for ecliptic latitudes $\leq 30^{\circ}$, and every $\sim 10^{\circ}$ above that. In addition to excluding observations within 10° of the Galactic plane, only "quiet" pixels which were not overtly situated on a strong photometric gradient were chosen for each wavelength. All available high quality weekly averages were used for each chosen line-of-sight; this translates to a maximum of 40 time samples (for pixels near the ecliptic poles) and an average of about 20 time samples for pixels near the ecliptic plane. No chosen line-of-sight had fewer than 8 time samples. Each wavelength used ~ 800 lines of sight after exclusion of the Galactic plane. The "quiet" pixel criterion did not constrain the ~ 800 lines

of sight to be precisely the same at each wavelength, since local photometric gradients are also wavelength dependent.

Further analysis showed that the relatively high detector noise and small contribution of the IPD signal at 140 and 240 μ m caused these bands to possess very little influence on the derived model geometry. In addition, the number of longer wavelength data points used in the fitting dataset was insufficient to overcome inherent random errors in these data. Ultimately, these data constraints forced adoption of a two-step fitting procedure. In the first step, the complete set of model parameters (geometry and source terms) were found simultaneously using data from the $1.25-100~\mu$ m wavelength bands. In the second step, the model geometry found for $1.25-100~\mu$ m was assumed to be applicable to the 140 and 240 μ m bands. In this case, the non-linear problem reduces to a linear least-squares solution for the 140 and 240 μ m model source terms. Rather than sampling the sky every few degrees, the complete DIRBE weekly dataset at these two wavelengths is used in a separate fit to derive the 140 and 240 μ m source terms, once again relying only upon temporal variations.

5. RESULTS

The result of the modelling process described above is a formulation which can be used to describe the modulations in the IPD foreground observed by DIRBE to an accuracy of 2% or better. This section describes the results of the fitting process, starting with the small subset of data used to produce the model, and working up to the production of maps of the full sky in which the zodiacal foreground has been removed based on our model. Consistency of the model with the observed modulation and observed structure in the IPD is also discussed in this section, whereas the question of the uniqueness of the model is addressed in \S 6.

5.1. Optimized Model

There are nearly 90 potential free parameters in this model, including both density terms and particle thermal emissivity and scattering properties. In the final optimization run, fewer than 50 of the parameters were actually determined from the fitting procedure. Treatment of the albedos and emissivities has been been discussed in § 4; in addition, some of the dust band and circumsolar ring density shape parameters were held fixed. This was necessitated in part by limitations in the fitting dataset, and in part because of deficiencies in the analytical model which would cause one density component to attempt to compensate for inadequacies in another.

The idea of using only the apparent time variation to determine the zodiacal light was tested on simulated DIRBE observations (including noise) of a model IPD cloud. The fitting procedure was able to recover the properties of the smooth cloud and circumsolar ring well. However, some angular variations of the low-contrast dust bands were difficult to recover, partly because of the large grid spacing in the fitting dataset. To remedy this, some of these parameters were set to values derived by Reach et al. (1997) using angular filtering techniques to isolate the dust band structure. In addition, tests on real data showed that the circumsolar ring component would sometimes be fit in a way that attempted to flatten it to compensate for the dust bands. For this reason, the parameters θ_{TB} and σ_{rSR} were fixed to values derived from visual examination of DIRBE data.

The final $1.25-100~\mu\mathrm{m}$ fitting dataset consisted of ~ 800 lines of sight per wavelength and a total number of 87,035 observations (including all wavelengths and weekly samples). This constitutes only $\sim 0.13\%$ of the weekly averaged dataset. There are 45 model parameters, leaving 80,425 degrees of freedom for the model fitting. Final parameter values are summarized in Tables 1 and 2, together with a short description of each parameter. Also listed is the 68% joint confidence uncertainty for each fitted parameter, which is derived from the maximum projection of the principal axis of the 45-parameter 68% confidence ellipsoid onto the axis for that individual parameter.

The final total χ^2 per degree of freedom for the optimized fit to the 1.25 – 100 μ m data was 2.1. The χ^2 per degree of freedom achieved for the individual bands from 1.25 to 100 μ m was 2.2, 1.9, 2.0, 3.6, 2.3, 1.5, 1.4 and 1.7, respectively. These reduced χ^2 's are higher than one would expect a priori. Some part of this excess appears to be due to the fact that the brightness of the IPD is intrinsically time dependent (see § 5.6), but this variation was not recognized until after the present modelling effort was completed. As discussed in § 5.6, the intrinsic time variation is small, and ignoring it in the model is not believed to have caused significant error in the residual sky brightness or the conclusions of our CIB search.

Though the formulation of the IPD modelling problem has been approached differently by various researchers, it is interesting to compare the findings for some of the major parameters. This is done in Table 3, where comparisons are made with five recent investigations.

5.2. Residuals within the Fitting Dataset

Figure 5 shows the IPD model brightness overlaid on the data for three pixels selected from the fitting dataset used to optimize the model parameters. The zodicacal model

intensity has been offset to match the mean observed pixel brightness, just as is done in order to fit the data. Within the error bars, the fit looks good on a pixel-by-pixel basis. Section 3 and Figure 3 provide an explanation of the shape of the intensity variation.

The character of the mean-adjusted residuals $[(I_{\lambda} - \langle I_{\lambda} \rangle) - (Z_{\lambda} - \langle Z_{\lambda} \rangle)]$ for the complete dataset used to fit the time variation is illustrated in Figure 6. The histograms in Figures 6ad show that the overall means of the residuals from the fit are very close to zero within a roughly Gaussian distribution function of narrow width. A search for systematic trends in the residuals versus ecliptic latitude and solar elongation is presented for 1.25, 3.5, 25 and 100 μ m in Figure 6. The 25 μ m trend with solar elongation shows some systematic structure, which is also seen at 12 μ m.

5.3. Residuals for a Weekly Map

The optimized DIRBE IPD model brightness was evaluated for each of the 41 Weekly Sky Maps described in § 2 using the model parameters (Tables 1 and 2) and equation 1. Figure 7 illustrates the IPD modelling results for one of these weekly maps (DIRBE mission week 22, which consists of averaged observations over the interval 1990 April 16-22, inclusive). For each pixel, the model was evaluated for the same time as the average time of observation of that pixel during the week. The results for the 25 μ m data are shown in order to illustrate most clearly deficiencies of the model. The observed sky brightness is presented in Figure 7a, and the corresponding IPD model intensity for this week is shown in Figure 7b on the same scale. The residual map which results from subtracting the IPD model from the data is provided in Figure 7c on a linear scale whose maximum is ~ 20 times fainter than that used to display the observed sky brightness. The brightest residual features are emission from the Galactic plane. There are, however, lower-level systematic residuals which arise from imperfections in the zodiacal model. The most noticable of these residual imperfections lie near the ecliptic plane and solar elongation extrema. An excess residual in the 12 and 25 μ m maps at solar elongation extrema was also indicated in the results for the fitting dataset described in \S 5.2.

Individual contributions to the IPD model brightness from the smooth cloud, dust bands, and circumsolar ring components are given in Figures 7d, 7e, and 7f, respectively. The intensity stretch for Figures 7e and 7f is expanded ~ 20 times compared to Figure 7d in order to show detail. The intensity from the circumsolar ring is asymmetric with respect to the Earth-leading and trailing halves of the sky; the brighter half corresponds to that containing the trailing "blob" ($\S 4.2.3$). Comparison of the residuals in Figure 7c with the individual component contributions in Figures 7d and 7f shows that some of the lower-

level structure in the residuals correlates with the dust bands and circumsolar ring intensity contours. There is an ecliptic plane excess in the leading half of the week 22 residual map near elongation 80°. The similarity of this excess to the brightness profile of the ring indicates that there is an insufficient model contribution from the circumsolar ring.

5.4. Average Residuals

Mission-averaged maps of the sky with zodiacal light removed were formed by averaging together the available weekly residual maps, of which Figure 7c is one example. Because of the imperfections in the IPD model at extreme solar elongation angles described previously, a solar elongation constraint was implemented by which weekly-averaged observations for which $e < 68^{\circ}$ and $e > 120^{\circ}$ were excluded from the average. In addition, data from three of the 41 weeks were excluded from the average for the $1.25-100~\mu m$ data because of low numbers of normal survey observations in those weeks (COBE DIRBE Explanatory Supplement, 1997).

Figure 2 shows the observed mission-averaged sky brightness at all 10 DIRBE wavelengths, in addition to the mission-averaged maps after zodiacal light removal. Mission-averaged maps which have had the IPD signal removed are shown on two scales — the first on the same logarithmic scale as the measured data, in order to illustrate the success of zodiacal light removal compared to the original signal (Fig. 2b). The second scale is a linear stretch chosen to emphasize any visible defects in low-intensity portions of the residual maps (Fig. 2c).

If the removal of the IPD signal were perfect, the mission-averaged residual maps would appear as clean images of the Galaxy and any extragalactic light. While the removal of the zodiacal signal in the near- and far-infrared looks relatively free of defects even on the expanded linear scale of Figure 2c, there are clearly systematic defects present in the $4.9-60~\mu m$ residual maps. These wavelengths present the most rigourous test of the IPD model, since it is at these wavelengths that the zodiacal foreground is strongest. In general, there are systematic residual features parallel to the ecliptic plane and within about 15° of it at these wavelengths. Such features presumably arise from deficiencies in the model. In general, these features are relatively faint. For example, the 12 μm excess near the ecliptic plane is of order 2% of the zodiacal signal.

5.5. Contribution of IPD Signal to Total Sky Brightness

The IPD model provides quantitative estimates of the contribution of the zodiacal foreground to the observed sky brightness at each of the ten DIRBE wavelengths. Figures 8 and 9 illustrate the observed sky intensity and corresponding IPD model intensity for representative directions in the sky. For regions not dominated by strong Galactic sources, the estimated fraction of the total sky brightness due to zodiacal light varies from about 2/3 in the near-infrared (1.25–3.5 μ m) to more than 90% in the mid-infrared (4.9–60 μ m). Even in the far-infrared, the zodiacal contribution is not completely negligible at high Galactic latitudes: $\sim 20\%$ of the 240 μ m emission in the "Lockman hole" (direction of minimum HI column density, Lockman et al. 1986) can be attributed to zodiacal emission, as shown in Figure 9b. The values used to make the plots in Figure 9 are also presented in Table 4, with further details about the locations in the figure caption.

Quantitative uncertainties associated with the IPD model are discussed in the following sections. These include both the errors associated with fitting the observed time dependence with the chosen model, as well as uncertainty in the true IPD brightness resulting from the fact that other model formulations might fit the time dependence of the observations equally well. This issue of model "non-uniqueness" is of critical importance for cosmological studies such as the search for the CIB. As a simple illustration, the zodiacal brightness at high ecliptic latitudes is influenced at the few-percent level by the modelled contribution of the near-Earth IPD structures. Changing the formulation for the 10° asteroidal bands so that they migrate in completely toward the Sun, rather than having an inner cut-off radius as in our model, increases the contribution for the dust bands shown in Figure 9b by a factor of 5 at high ecliptic latitude. A change in the band inner cut-off has little effect on the model at low ecliptic latitudes. Changes in the residual sky brightness resulting from different inner radial cut-offs for the bands are within the uncertainties of the isotropic components of the IPD model discussed in § 6.

5.6. Consistency of Model as a Function of Time

It is difficult to specify precisely the errors inherent in our modelling technique of fitting the time variations of the sky brightness. This is particularly true because the level and nature of the errors depend both on epoch and spatial location. To give some insight on this point, Figure 10 presents maps of the 12 μ m sky brightness in ecliptic coordinates for four weeks during the mission. These weeks have been selected so that two of the maps were obtained approximately one-half year after one of the earlier maps. Data at 12 μ m were used because the IPD signal is the predominant signal in the sky and because all features in

the model are evident in the data. These specific images are "constant-time maps" created by interpolating linearly between contiguous weekly-averaged maps (in which the mean time of observation of each pixel is not a constant, but depends upon the times in which it was scanned during that week). In "constant-time" maps the brightness at each pixel represents a view of the IPD cloud at a fixed time, thus eliminating the small brightness fluctuations in our Weekly Sky Maps arising from different mean observation times per pixel.

These constant-time maps have been used to create Figure 11, which shows the variation of the brightness of the sky, the IPD model, and the residuals (difference between measured brightness and model) as a function of ecliptic longitude for two representative latitudes. This figure also shows the average of the weekly residual results. Both the sky maps and line plots disclose much about the nature of the modelling errors.

Comparing the maps separated by half a year shows that the residuals in the ecliptic polar regions are quite comparable, but there are clear indications of variable errors in the vicinity of the ecliptic plane. Note in particular the large-scale inversions of the strength of the residuals between maps separated by half a year in the center portion of the maps. This results mainly from an inadequate representation of the circumsolar ring and the Earth-trailing blob. Errors resulting from deficiencies in the model of the dust bands are also visible. While the errors can be easily seen in these maps, it is essential to realize that these obvious artifacts result from modelling errors which are only a few percent of the intensity of the zodiacal emissions. But the nature of the errors is complex; some features of this complexity are illuminated by the latitude-cut line plots of Figure 11.

In the plots for $\beta=80^{\circ}$, it is seen that the longitudinal dependence of the zodiacal emission is seemingly very well tracked by the model. But there is a noticeable phase shift between the observations and the model. This phase difference is vividly translated into a wide separation of residuals over a half-year interval. Though not shown graphically, for weeks 6 and 32 this separation reaches a maximum around longitude 180°, whereas for weeks 12 and 38 the peak separation appears around longitude 240°. The cause of this temporal variation in the phase shift between the observations and the model is not known.

The model does reproduce well the striking differences in the amplitude of the time variation of the IPD signal in different directions. For example, in the data of weeks 6 and 32, the variation in the sky at a latitude of 80° for longitude of 100° is ~ 0.1 MJy sr⁻¹. This is in contrast to the observations at 270° where the variation is ~ 3.7 MJy sr⁻¹. The range of temporal variation at high latitudes is strongly dependent on longitude. That the model captures this distinctive feature of the temporal variation indicates that the basic geometry of the IPD cloud is represented reasonably well in the model. A comparison of the weekly results with the mission-averaged values indicates that the error in the modelled zodiacal

contribution ranges from 0 to 4% of the IPD modelled brightness, implying an error in the average residual ranging from about 0 to 42%.

The plots for $\beta=0^\circ$ demonstrate what can be seen in the corresponding full-sky maps — there are strong anti-correlated variations in the residuals separated by one-half year. All elements of the model, i.e., main cloud, circumsolar ring, and bands, combine to produce these effects. Though the residuals behave quite differently in the two halves of the year, it should be noted that the differences in the residuals only represent a modest lack of fidelity in the model, ranging from about 0 to 3.8% of the IPD brightness in a pixel.

The characteristics of the DIRBE data set which make it well-suited for modelling of the IPD signal based upon the observed time variation of the sky brightness (highly repetitive sampling, stable photometry) also permit some unique analyses of the global deficiencies in the modelling. One of the best methods for discerning the general nature of the model defects over the whole sky comes from an analysis of the weekly residuals maps. As noted above, a grand residual sky map was produced at each wavelength by subtracting the weekly map calculated from the IPD model from the map of weekly-averaged observations, and then averaging these weekly residual maps over all the weeks of the mission as described in § 5.4. Using the average residual map as a fiducial measure, a distribution function representing the quality of each weekly residual map was constructed by forming the difference between the weekly residual map and the mission-averaged residual map, expressed as a fraction of the IPD model brightness for that week:

$$\{[I_{\lambda}(w,p) - Z_{\lambda}(w,p)] - \langle I_{\lambda}(w,p) - Z_{\lambda}(w,p)\rangle_{w}\}/Z_{\lambda}(w,p), \tag{11}$$

where this expression is evaluated for each visible pixel p in the weekly map. If the modelling were perfect, the distribution functions of these weekly pixel differences would be Gaussians with mean zero.

Using again the 12 μ m data for illustration, Figure 12 shows two examples of such distribution functions for mission weeks 12 and 38. These distribution functions are created after removing the bottom and top 0.5% of the data to remove the effects of discrepant outliers. The number of pixels contributing to such distribution functions is a bit more than those in half the sky, i.e., about 205,000 per week. As can be seen in Figure 12, the distribution for week 12 is not Gaussian whereas the distribution for week 38 is nearly Gaussian. These two examples also illustrate that the means of the distribution functions are not stable with time. This instability in the means is shown in Figure 13, where the time variation of the means of the weekly distribution functions are shown for the 1.25, 3.5, 12, and 240 μ m data. A five-term harmonic fit to the means with a one-year period is also shown. The use of a one-year fitting period is based on the conclusion that one problem with the model arises from assuming the circumsolar ring to be circular, whereas the orbit

of the Earth about the Sun is eccentric. It is interesting to note that the phase of the fit for the 12 μ m data is almost 180 degrees out of phase with those for the other wavelengths. It is believed that this could be caused by the strong dependence of the 12 μ m result on the assumed model structure for the circumsolar ring and trailing blob.

The plots in Figure 13 also show a high frequency variation of the means, with a period of the order of 27 days and an amplitude of 1-2%. Such variations are not seen in the photometry of the discrete standard objects used to stabilize our photometric system on long time scales, so they are not artifacts arising from the calibration process. Such variations are also seen in the average behavior of the deviations of subsets of isolated pixels relative to harmonic fits of the observations, i.e., it is not a phenomenon arising only in some special direction(s) in the sky or from the modelling of the IPD cloud. It is most strongly seen in the $4.9 \mu \text{m}$ data. The approximate 27 day period suggests a cause related to the Moon or to solar rotation. Since the Moon crosses the DIRBE scan swath twice per lunar month, any lunar effect would be expected to have a 14 day period. Furthermore, the DIRBE off-axis response was measured in flight and found to be orders of magnitude less at all angular distances from the Moon retained in the DIRBE data analysis than the residual effects seen in Figure 13. A more likely cause is therefore solar modulation of the zodiacal light brightness due to solar rotation and variation of the UV flux associated with sunspots. This is supported by the fact that the variations are correlated with the Mg II absorption strength. A similar UV-flux variation periodicity is seen in the sky Ly- α background (Quémerais, Sandel & de Toma 1996). A more thorough discussion of this discovery will be presented in a separate paper (Kelsall et al. 1998). Although low- and high-frequency variations are evident in the residuals, these effects are small, and the modelling results at all wavelengths reproduce the mean behaviour of the observed sky to within a few percent of the level of the IPD contribution. Table 5 summarizes the deviations of the weekly residual sky maps from the mission-averaged residual sky maps, as illustrated in Figure 12. Table 5 also shows similar statistics for the high quality region B used in our search for the CIB (Paper III).

6. Uncertainties in Cosmological Results

The uncertainties and errors in the model of the IPD thermal emission and scattered light can be characterized in many different ways; e.g., measurements of residual variations as a function of time, or amount of residual emission that is correlated with components of the IPD model. The errors evident as temporal variations of the residual emission are reduced by averaging the data over time for the length of the DIRBE cold-era mission. Model errors that are apparent as residual structure in the maps can often be minimized by selection of

"good" regions of the maps (typically at high latitude) for use in further analyses. However, since we ultimately seek to determine the level of an isotropic CIB, the most significant form of uncertainty is that which affects the amount of emission from any potential isotropic or nearly-isotropic IPD component. This is an issue of model uniqueness: Are there any other models that can give an equally good fit to the apparent time variations of the IPD emission and scattered light, and yet lead to substantially different isotropic residuals?

To evaluate the uncertainty of a CIB measurement due to the uncertainty in the isotropic or nearly-isotropic components of the IPD model, we attempted to fit the IPD cloud using several different functional forms (kernels) for the density distribution of the main IPD cloud. The intensity differences between models which fit the time variations equally well are taken as a measure of the uncertainty in the IPD model.

For this analysis, the shape and position of the small scale components of the IPD were fixed, except for the inclination and line of nodes of the 10° dust bands. Functional forms for the main cloud that were tested included the IRAS model (Wheelock et al. 1994), a modified fan model, an ellipsoid model, a sombrero model (Giese et al. 1986) and a widened modified fan model (eqs. 6 and 7). Each of the models was used to fit the time variations of the $1.25-100~\mu m$ intensities at one pixel in each $5^{\circ} \times 5^{\circ}$ patch of the sky. Regions within 10° of the Galactic plane were excluded. In other respects the fitting of each model was performed in a manner similar to that described in § 4.3. In general the differences between the models are encouragingly small, being of the order of a few percent. This is illustrated in Table 6, where the relative values of the sky brightness as a function of model is shown for the north Galactic pole.

For the sample of functional forms described above, the total χ^2 per degree of freedom across all fitted wavelengths was comparable for the modified fan ($\chi^2=2.292$), the widened modified fan ($\chi^2=2.273$), and the ellipsoid ($\chi^2=2.253$) models. The *IRAS* and sombrero models fared distinctly worse at $\chi^2=2.562$ and 3.187, respectively. The model intensities were evaluated at five high-latitude regions of interest for measurement of the CIB (Paper I): the north and south ecliptic poles, the north and south Galactic poles, and the Lockman hole region, which contains the location of lowest Galactic H I column density. Among the three models with the lowest χ^2 , the largest intensity differences were found at the NGP region. At wavelengths from 1.25 – 100 μ m the ellipsoid model was brighter than the widened modified fan model, which was brighter than the modified fan models. Thus, we have taken the differences between the ellipsoid and the modified fan models at the NGP as an indication of the uncertainty in the IPD models. These uncertainties are listed in Table 7. The uncertainties at 140 and 240 μ m were obtained by scaling the 100 μ m uncertainty by the mean color of the IPD emission at 100 μ m relative to the emission at 140 and 240 μ m,

respectively.

By choosing the *largest* variations among good IPD models at high latitudes, we may be overestimating the uncertainty of the IPD model at a *typical* high latitude location. However, we cannot be certain that there are not other models of the IPD cloud that can fit the time variation of the data as well as the models we have investigated, and yet lead to larger differences in the predicted model intensity. Most important, the existence of a real isotropic component in the IPD contribution to the sky brightness which is not represented in any of these semi-empirical models cannot be discerned directly by fitting the time variation in the DIRBE data. Independent arguments limiting the likely intensity of such a component are made in Paper IV and summarized in Paper I.

An additional systematic error that needs to be recognized arises from the fact that, as noted in § 5.6, the weekly mean deviations of the residual sky maps (after the modelled IPD contribution is removed) from the mission-averaged residual map show a strong harmonic feature with a period of 1 year. Since the DIRBE observations did not cover a full year, averaging this harmonic variation over an incomplete cycle introduces a small systematic "truncation" error. These errors have been computed for both the whole sky and a smaller region used for the analysis in Paper I. Since the main cosmological results of Paper I are based upon small selected areas of the sky, it is important to check whether the magnitude of the error seen for the whole sky applies to these selected areas. A study of the distribution functions of the deviations of the weekly residuals was performed for the "High Quality Region B (HQB)", which contains two patches at high northern and southern Galactic and ecliptic latitudes. The variation of the means of these distribution functions is similar to that for the whole sky. The grand average of these weekly means has a truncation error of about one percent or less of the IPD contribution, except at 240 μ m, as shown in Table 8. The truncation error has a generally small impact on the overall uncertainties of the IPD model at every DIRBE wavelength.

7. CONCLUSIONS

This paper describes in some detail the construction of a physically motivated, parametric model of the IPD cloud contribution to the infrared sky brightness using the most distinctive and only unique feature of that contribution: its apparent temporal variation in fixed celestial directions induced by the orbiting of the Earth about the Sun. The effort to arrive at a model satisfactory for our search for the cosmic infrared background (CIB) turned out to be more arduous than expected, since the data revealed the complex cloud structures not known when the DIRBE investigation was planned. The model presented

here is the survivor from a large number of parameterizations and fitting procedures which we have investigated. This extensive effort, while time consuming, was essential since it was driven by the desire to achieve an $\sim 1\%$ precision in the identification of the IPD signal. It is critical to note that "precision" is the correct word, for though the model well represents the time variations, it is not a unique model. It is, in fact, impossible to determine a unique model from any set of data taken from within the IPD cloud. Only a mission flying well beyond the orbit of Jupiter could gather data permitting a unique solution.

Though not unique, the model described here is of rather high fidelity, in that it reproduces the apparent time variations over the sky and leaves quite stable residual maps at all wavelengths. The range of functional forms investigated allows an estimate of the uncertainties due to the lack of uniqueness of the final model. The modest size of these uncertainties has allowed successful conduct of our search for the CIB (Paper I). The resulting residual maps with the IPD contribution removed are the best all-sky absolutely-calibrated photometric maps now available for study of large-scale Galactic phenomena from 1.25 to $240~\mu m$, though evident artifacts do remain, especially at low ecliptic latitude.

The virtues of our approach for finding the contribution of the IPD cloud to the infrared sky brightness include the following:

- Modelling the time variations only is a unique method which does not require extraneous zero point constants, and automatically excludes contributions from Galactic or extragalactic sources.
- Modelling using the data from many wavelengths simultaneously provides an IPD structure which is consistent with the data and the same for all wavelengths.
- The IPD cloud density function kernel found by modelling the time variations produces a level for the IPD contributions over two orders of magnitude in wavelength which are compatible with expectations, i.e., that a positive sky residual remains after removing the modelled IPD contribution.
- The isotropic part of the model is only modestly sensitive to the functional forms chosen to parameterize the model.
- The method readily permits incorporation of all known elements of the IPD cloud: a main cloud, the asteroidal bands, and a circumsolar ring containing dust particles in Earth-resonant orbits near 1 A.U.
- The model yields a global precision of the order of a few percent of the IPD contribution.

• Because the IPD cloud contains reasonably smooth features, the method is efficient in that a robust IPD model can be constructed using only a very limited fraction ($\sim 0.13\%$) of the DIRBE data set.

Though our approach produced a successful model for the IPD cloud, it is also clear that it is not a perfectly consistent model for the whole sky. Testing the time stability of the weekly residual sky maps after subtracting the modelled IPD contribution is a powerful tool for assessing the quality of the model. The result of that assessment is that the model did achieve the goal of matching the time variations. There are, however, apparent spatial artifacts in the results that are correlated with the various components of the IPD cloud and quite clearly reflect imperfections in the model. On the basis of this work, we feel that further improvements could be made in constructing a quasi-physical model that, without recourse to elaborate representations of the dust, should be able to achieve further improvements in the results.

Some possible changes in the modelling technique, in rough order of perceived priority, are as follows:

- Force the trailing blob in the circumsolar ring to trail the Earth in its eccentric orbit;
- Include a separate contributing form factor for the dust coming from the main-belt asteroids;
- Incorporate more realistic representations for the asteroidal bands and the circumsolar ring, where now, for example, the representations use simple Gaussian distributions;
- Include a source function scattering term at 4.9 and 12 μ m since a significant fraction of the IPD particles are large enough to scatter these wavelengths efficiently;
- Recognize a possible warpage of the symmetry plane as a function of distance from the Sun due to the influences of Jupiter, Mars, Earth, and Venus;
- Include an intrinsic time variation of the IPD brightness with a period equal to that seen in the data;
- Permit variation of the albedo for the shorter wavelength bands to accommodate the clues in the observations that point to a variation with latitude, which may well result from the differences in the dust contributed by comets as compared to that coming from asteroids;
- Add a contribution from a hot dust component; and,

• Incorporate the deviations from the grand average residuals directly into an iterative modelling loop so as to limit the available solution space and push the results towards distribution functions of residuals which are Gaussian.

The data described in this paper are available to the public from the NSSDC through the COBE website at http://www.gsfc.nasa.gov/astro/cobe/. The DIRBE weekly maps of the sky and the corresponding IPD model brightness are available as the "DIRBE Sky and Zodi Atlas (DSZA)" product; the mission-averaged, zodi-subtracted residual skymaps are contained in the "Zodi-Subtracted Mission Average (ZSMA)" maps.

The authors gratefully acknowledge the contributions over many years of the many engineers, managers, scientists, analysts, and programmers engaged in the DIRBE investigation. The National Aeronautics and Space Administration/Goddard Space Flight Center (NASA/GSFC) was responsible for the design, development, and operation of the *COBE*. Scientific guidance was provided by the *COBE* Science Working Group. GSFC was also responsible for the development of the analysis software and for the production of the mission data sets.

REFERENCES

- Arendt, R. G., Odegard, N., Weiland, J. L., Sodroski, T. J., Hauser, M. G., Dwek, E., Kelsall, T., Moseley, S. H., Silverberg, R. F., Leisawitz, D., Mitchell, K., & Reach, W. T. 1998, ApJ, submitted (Paper III)
- Baguhl, M., et al. 1995, Science, 268, 1016
- Banaskiewicz, M., Fahr, H. J. & Scherer, K. 1994, Icarus, 107, 358
- Beichman, C. A. 1987, ARA&A, 25, 521
- Berriman, G. B., et al. 1994, ApJ, 431, L63
- Bevington, P. R. 1969, "Data Reduction and Error Analysis for the Physical Sciences," (McGraw Hill), p.237
- Boggess, N. et al. 1992, ApJ, 397, 420
- Boulanger, F. & Perault, M. 1988, ApJ, 330, 964
- COBE Diffuse Infrared Background Experiment (DIRBE) Explanatory Supplement, ed. M. G. Hauser, T. Kelsall, D. Leisawitz, and J. Weiland, COBE Ref. Pub. No. 97-A (Greenbelt, MD: NASA/GSFC), available in electronic form from the NSSDC.
- Cassini, J-D. 1685, Mem. de l'Acad. Roy. Sci., Tome viii
- Dermott, S. F., Nicholson, P. D., Burns, J. A. & Houck, J. R. 1984, Nature, 312, 505
- Dermott, S. F., Jayraraman, S., Xu, Y. L., Gustafson, B. Å. S. & Liou, J. C. 1994, Nature, 369, 719
- Dermott, S. F., Jayraraman, S., Xu, Y. L., Grogan, K., & Gustafson, B. Å. S. 1996, in "Unveiling the Cosmic Infrared Background," ed. E. Dwek (New York:AIP), p. 25
- Deul, E. R. & Wolstencroft, R. D. 1988, A&A, 196, 277
- Divine, N. 1993, J. Geophys. Res., 98, 17029
- Durda, D. D. & Dermott, S. F. 1997, Icarus, 130, 140
- Dwek, E., Arendt, R. G., Hauser, M. G., Fixsen, D., Leisawitz, D., Pei, Y.C., Wright, E. L., Kelsall, T., Mather, J. C., Moseley, S. H., Odegard, N., Shafer, R., Silverberg, R. F., & Weiland, J. L. 1998, ApJ, submitted (Paper IV)
- Fahr, H. J., Scherer, K. & Banaskiewicz, M. 1995, Planet. Space Sci., 43, 301
- Franz, B. A. et al. 1996, in "Unveiling the Cosmic Infrared Background," ed. E. Dwek (New York: AIP), p. 296
- Giese, R.H., Kneissel, B. & Rittich, U. 1986, Icarus 68, 395

Gold, T. 1975, Nature, 25, 489

Grogan, K., Dermott, S. F. & Gustafson, B. Å. S. 1996, ApJ, 472, 812

Haug, U. 1958, Z. Astrophys., 44, 71

Hauser, M.G. 1988, in *Comets to Cosmology*, Proc. of the Third IRAS Conf., ed. A. Lawrence (Springer-Verlag), pp. 27.

Hauser, M. G., Arendt, R. G., Kelsall, T., Dwek, E., Odegard, N., Weiland, J. L., Freudenreich, H. T., Reach, W. T., Silverberg, R. F., Moseley, S. H., Pei, Y.C., Lubin, P., Mather, J. C., Shafer, R., Smoot, G. F., Weiss, R., Wilkinson, D. T. & Wright, E. L. 1998, ApJ, submitted (Paper I)

Hong, S. S. 1985, A&A, 146, 67

Jackson, A. A. & Zook, H. A. 1989, Nature, 327, 629

Jones, M. H. & Rowan-Robinson, M. 1993, MNRAS, 264, 237

Kelsall, T., et al. 1993, Proc. SPIE Conf. 2019, Infrared Spaceborne Remote Sensing, ed. M. S. Scholl (Bellingham: SPIE), 190

Kelsall, T., et al. 1998, in preparation

Leinert, Ch., Link, H., Pitz, E. & Giese, R. H. 1976, A&A, 47, 221

Leinert, Ch. et al. 1998, A&AS, to be published

Liou, J. C., Dermott, S.F. & Xu, Y. L. 1995, Planet. Space Sci., 43, 717

Lockman, F. J., Jahoda, K., & McCammon, D. 1986, ApJ, 302, 432

Low, F. J. et al. 1984, ApJ, 278, L19

Marzari, F. & Vanzani, V. 1994a, A&A, 283, 275

Marzari, F. & Vanzani, V. 1994b, Planet. Space Sci., 42, 101

Murdock, T. L. & Price, S. D. 1985, AJ, 90, 375

Neugebauer, G. et al. 1984, ApJ, 278, L1

O'Neill, E. M., & Laubscher, R. E. 1976, Extended Studies of a Quadrilateralized Spherical Cube Earth Data Base, (NEPRF Technical Report 3-76) (NTIS Report AD-A026294) (Computer Sciences Corp. CSC/TR-76/6008)

Quémerais, E., Sandel, B. R. & de Toma, G. 1996, ApJ, 463, 349

Reach, W. T. 1988, ApJ, 335, 468

Reach, W. T. 1992, ApJ, 392, 289

Reach, W. T. et al. 1995, Nature, 374, 521

Reach, W. T. et al. 1996, in "Unveiling the Cosmic Infrared Background," ed. E. Dwek (New York: AIP), p. 37.

Reach, W. T. et al. 1997, Icarus, 127, 461

Rowan-Robinson, M., et al. 1990, MNRAS, 246, 273

Schramm, L. S., Brownlee, D. & Wheelock, M. M. 1989, Meteoritics, 24, 99

Silverberg, R. F. et al. 1993, Proc. SPIE Conf. 2019, Infrared Spaceborne Remote Sensing, ed. M. S. Scholl (Bellingham: SPIE), 180

Spiesman, W. J. et al. 1995, ApJ, 442, 662

Staubach, P., Divine, N. & Grün, E. 1993, Planet. Space Sci., 41, 1099

Struve, O. 1943, ApJ, 98, 129

Sykes, M. V., Lebofsky, L. A., Hunten, D. M., & Low, F. 1986, Science 232, 1115

Sykes, M. V., Greenberg, R., Dermott, S. F., Nicholson, P. D., Burns, J. A., & Gautier, T. N., Jr. 1989, in *Asteroids II*, eds. R. P. Binzel, T. Gehrels, & Matthews (Tucson: U. Arizona), p. 336

Wheelock, S. L. et al. 1994, "IRAS Sky Survey Atlas Explanatory Supplement," JPL Publication 94-11 (Pasadena: JPL)

This preprint was prepared with the AAS LATEX macros v4.0.

- Fig. 1.— DIRBE 12 μ m maps of the sky for various integration periods: a) one orbit; b) one day; c) one week; d) 10 months. Maps are Mollweide projections in ecliptic coordinates.
- Fig. 2.— DIRBE mission-averaged sky brightness in 10 wavebands, both before and after removal of the IPD signature: a) as-observed sky, logarithmic scale; b) sky after removal of ZL, scaled identically with a); c) same as b), but on a linear scale expanded to show defects in the residuals. Units are in MJy sr⁻¹. Sixteen color contour levels are used. The minimum and maximum scaling values used for each band are listed as follows, with the first set of numbers being the logarithmic scaling limits, and the second set being the linear scale: 1.25 μ m: [.063,31.6], [-0.05,0.3]; 2.2 μ m: [0.04,31.6], [0,.2]; 3.5 μ m: [0.032,31.6], [-0.01,.2]; 4.9 μ m: [0.1,15.8], [0,0.2]; 12 μ m: [1.58,79.4], [0,2]; 25 μ m: [3.98,79.4], [0.5,3]; 60 μ m:[1,79.4], [0,3]; 100 μ m: [1,79.4], [0,15]; 140 and 240 μ m: [1,794.3], [0,20]. All maps are Mollweide projections in ecliptic coordinates.
- Fig. 3.— Schematic representation of zodiacal light brightness vs. time as observed by DIRBE at the: a) north ecliptic pole and b) ecliptic plane. In a), the dust cloud is represented as a shaded ellipse which is tilted with respect to the plane of the Earth's orbit. (See text for additional explanation.)
- Fig. 4.— Isodensity contours of the IPD Model Components, shown for a cross-sectional slice perpendicular to the ecliptic plane: a) all components combined; b) smooth cloud; c) dust bands; d) circumsolar ring. The density contour levels used in a) and b) are listed in brackets at the bottom of a), in units of 10^{-7} AU⁻¹. Contour levels used for c) and d) are a factor of eight smaller.
- Fig. 5.— Sky brightness vs. time as observed by DIRBE for 4 different wavebands and three different sky locations: a) the north ecliptic Pole; b) the north Galactic pole and c) the ecliptic plane (near ecliptic longitude 180°). Error bars include random and systematic uncertainties. Smooth curve through the data is that generated from the IPD model, with an offset added to raise the zodiacal contribution to the mean of the observed pixel photometry.
- Fig. 6.— Overall character of residuals in the fitting dataset for four representative wavelengths: a) 1.25 μ m, b) 3.5 μ m, c) 25 μ m and d) 100 μ m. For each wavelength band, the histogram of residuals, residuals as function of ecliptic latitude and residuals as function of solar elongation are plotted from bottom to top.
- Fig. 7.— Data, IPD model and residual maps for Week 22 (90106-90112) at 25 μ m: a) the as-observed sky. The scale is linear: [0,100] MJy sr⁻¹; b) sky brightness for this week as predicted by the IPD model, on the same scale as a). The IPD model intensities shown here are broken down into the brightness due to the smooth cloud, bands, and ring in d), e), and

- f), respectively; c) the residual map (observed model), on a linear scale [0,5] MJy sr⁻¹; d) Brightness for the smooth cloud model component, on the same scale as a); e) Brightness for the combined bands components, scale=[0,5.5]; f) Brightness for the ring model component, scale=[0,5.5]. All maps are Mollweide projections in ecliptic coordinates.
- Fig. 8.— IPD contribution to the observed sky brightness. The lower curve in each plot is the ZL brightness for the time and locations computed using the DIRBE IPD model. a) DIRBE observations of the infrared sky brightness on 1990 Jan 19 at solar elongation = 90°, ecliptic longitude 179°. The 140 and 240 μ m data have been averaged and smoothed. b) Mission-averaged intensity profile in the Galactic plane.
- Fig. 9.— Spectral energy distribution of the observed sky vs. the IPD model. The contributions from individual density components of the zodiacal cloud are also indicated. a) for DIRBE pixel 162811, located on the ecliptic plane at ecliptic longitude 122°. The time of observation is ~day 109 of 1990, corresponding to a solar elongation of approximately 90°. b) for DIRBE pixel 64552, located within the Lockman Hole (the region of minimum HI column density): ecliptic coordinates (137°,46°); Galactic coordinates (148°,53°). The time of observation is ~day 129 of 1990, corresponding to a solar elongation of approximately 90°. (See Table 4 for the numerical values.)
- Fig. 10.— DIRBE 12 μ m (data-model) residual maps for mission week pairs spaced 6 months apart: Weeks 6 and 32 (10a,b) correspond to mid-week observations times of 28 Dec 1989 and 28 Jun 1990, respectively, and are displayed on a linear stretch of [.456,3.511] MJy/sr. Similarly, weeks 12 and 38 (10c,d) correspond to 8 Feb 1990 and 9 Aug 1990, respectively, and the scale = [.439,3.987] MJy/sr. Maps are Mollweide projections in ecliptic coordinates.
- Fig. 11.— The 12 μ m intensity profiles as a function of ecliptic longitude for ecliptic latitudes of 80° (11a) and 0° (11b). For each latitude the top two panels show the sky data for two weeks separated by 26 weeks, while the next two panels show the corresponding data from the IPD model. The bottom panel shows an overlay of the differences of the sky and IPD model for each of the two weeks, as well as the run of the mission-average residual.
- Fig. 12.— Representative distribution functions of the ratio $\{[I_{\lambda}(w,p) Z_{\lambda}(w,p)] \langle I_{\lambda}(w,p) Z_{\lambda}(w,p)\rangle_w\}/Z_{\lambda}(w,p)$ where $\langle I_{\lambda}(w,p) Z_{\lambda}(w,p)\rangle_w$ is the mission averaged value. (a) shows the result for mission week 12 and (b) shows the same result for week 38; i.e., one displaced by 1/2-year where the expectation would be for similar results, which clearly are not obtained.
- Fig. 13.— Samples of the run of the full-sky mean for the $\{[I_{\lambda}(w,p) Z_{\lambda}(w,p)] \langle I_{\lambda}(w,p) Z_{\lambda}(w,p)\rangle_w\}/Z_{\lambda}(w,p)$ ratio as a function of time for the a) 1.25, b) 3.5, c) 12

and d) 240 μm bands.

Table 5. Deviations of the Weekly Residual Maps from the Mission-Averaged Residual Maps (see equation 11)

Region	Band (μm)	$\langle Mean \rangle$ (%)	$\langle Mean \rangle \ (\%)$	$\langle Median \rangle$ (%)		
Full Sky	Sky 1.25 0.07 ± 1.76		1.49 ± 1.77	0.11 ± 1.27		
	2.2	0.04 ± 0.92	0.73 ± 0.92	0.09 ± 0.60		
	3.5	-0.11 ± 1.59	1.26 ± 1.59	-0.04 ± 1.09		
	4.9	0.35 ± 1.07	0.88 ± 1.12	0.17 ± 0.92		
	12	0.30 ± 0.68	0.57 ± 0.74	0.17 ± 0.71		
	25	0.20 ± 0.30	0.28 ± 0.36	0.11 ± 0.30		
	60	0.10 ± 1.25	0.99 ± 1.26	0.07 ± 1.05		
	100	0.52 ± 4.10	2.74 ± 4.14	0.03 ± 2.45		
	140	0.82 ± 12.85	9.00 ± 12.88	0.24 ± 10.11		
	240	0.77 ± 21.22	16.6 ± 21.23	1.23 ± 16.38		
High	1.25	1.34 ± 2.63	1.41 ± 2.07	0.99 ± 2.54		
Quality	2.2	1.04 ± 1.44	0.53 ± 0.91	0.70 ± 1.47		
Region B	3.5	1.64 ± 1.96	0.88 ± 1.28	0.46 ± 2.39		
	4.9	1.60 ± 1.70	0.83 ± 1.37	0.75 ± 2.21		
	12	0.84 ± 1.07	0.37 ± 0.59	0.68 ± 1.21		
	25	0.65 ± 0.82	0.42 ± 0.55	0.53 ± 0.94		
	60	0.75 ± 1.54	0.75 ± 0.98	0.38 ± 1.68		
	100	1.51 ± 2.87	1.07 ± 1.68	0.49 ± 3.16		
	140	4.90 ± 13.51	6.29 ± 8.16	-0.54 ± 18.51		
	240	13.02 ± 31.31	11.38 ± 15.70	-0.22 ± 40.55		

Table 6. Relative IPD Cloud Brightness at the North Galactic Pole as a Function of Model Type

Wavelength (µm)	Present Model	Modified Fan Model	Widened Modified Fan Model	Ellipsoidal Model
1.25	1.00	1.05	1.06	1.08
2.2	1.00	1.11	1.12	1.14
3.5	1.00	1.00	1.00	1.03
4.9	1.00	1.01	1.01	1.03
12.	1.00	0.98	0.98	1.00
25.	1.00	0.97	0.98	1.01
60.	1.00	0.94	0.95	0.99
100.	1.00	0.93	0.95	1.00

Table 7. IPD Model Uncertainties for the CIB

Wavelength (μm)	Uncertainty (nW m $^{-2}$ sr $^{-1}$)
1.25	15
2.2	6
3.5	2.1
4.9	5.9
12	138
25	156
60	26.7
100	6.3
140	2.3
240	0.5

Table 8. Truncation Error in the High Quality Region B

Wavelength (μm)	Northern Patch (%)	Southern Patch (%)
1.2	1.1	1.6
2.2	0.3	1.2
3.5	0.8	0.2
4.9	1.1	0.4
12	0.6	1.1
25	0.4	0.9
60	0.1	1.0
100	-0.3	1.6
140	-0.7	1.9
240	-5.4	1.4

cloud component	parameter	description	final value	68% joint. conf. unc.
All	T_0	Temperature at 1 AU	$286~\mathrm{K}$	fixed
	δ	Temperature power law exponent	0.467	0.0041
	$C_{0,1}$	$1.25\mu m$ phase func. parameter	-0.942 sr^{-1}	fixed
	$C_{1,1}$	$1.25\mu\mathrm{m}$ phase func. parameter	$0.121 \text{ rad}^{-1} \text{ sr}^{-1}$	fixed
	$C_{2,1}$	$1.25\mu m$ phase func. parameter	-0.165 rad^{-1}	fixed
	$C_{0,2}$	$2.2\mu\mathrm{m}$ phase func. parameter	-0.527 sr^{-1}	fixed
	$C_{1,2}$	$2.2\mu\mathrm{m}$ phase func. parameter	$0.187 \text{ rad}^{-1} \text{ sr}^{-1}$	fixed
	$C_{2,2}$	$2.2\mu\mathrm{m}$ phase func. parameter	-0.598 rad^{-1}	fixed
	$C_{0,3}$	$3.5\mu\mathrm{m}$ phase func. parameter	-0.431 sr^{-1}	fixed
	$C_{1,3}$	$3.5\mu\mathrm{m}$ phase func. parameter	$0.172 \text{ rad}^{-1} \text{ sr}^{-1}$	fixed
	$C_{2,3}$	$3.5\mu\mathrm{m}$ phase func. parameter	-0.633 rad^{-1}	fixed
Smooth Cloud	A_1	Albedo, $1.25\mu\mathrm{m}$.204	0.0013
	A_2	Albedo, $2.2\mu\mathrm{m}$.255	0.0017
	A_3	Albedo, $3.5\mu\mathrm{m}$.210	0.019
	E_3	Emissivity mod. factor, $3.5\mu m$	1.66	0.088
	E_4	Emissivity mod. factor, $4.9\mu m$	0.997	0.0036
	E_5	Emissivity mod. factor, $12\mu m$	0.958	0.0026
	E_6	Emissivity mod. factor, $25\mu m$	1.00	fixed
	E_7	Emissivity mod. factor, $60\mu m$	0.733	0.0055
	E_8	Emissivity mod. factor, $100\mu m$	0.647	0.012
	E_9	Emissivity mod. factor, $140\mu m$	0.677	-
	E_{10}	Emissivity mod. factor, $240\mu m$	0.519	-
Dust Bands	A_1	Albedo, $1.25\mu\mathrm{m}$.204	fixed to smooth cloud
	A_2	Albedo, $2.2\mu\mathrm{m}$.255	fixed to smooth cloud
	A_3	Albedo, $3.5\mu\mathrm{m}$.210	fixed to smooth cloud
	E_3	Emissivity mod. factor, $3.5\mu m$	1.66	fixed to smooth cloud
	E_4	Emissivity mod. factor, $4.9\mu m$	0.359	0.054
	E_5	Emissivity mod. factor, $12\mu m$	1.01	0.15
	E_6	Emissivity mod. factor, $25\mu m$	1.00	fixed
	E_7	Emissivity mod. factor, $60\mu m$	1.25	0.30
	E_8	Emissivity mod. factor, $100\mu m$	1.52	0.65
	E_9	Emissivity mod. factor, $140\mu m$	1.13	-
	E_{10}	Emissivity mod. factor, $240\mu m$	1.40	=
Ring + Blob	A_1	Albedo, $1.25\mu\mathrm{m}$.204	fixed to smooth cloud
	A_2	Albedo, $2.2\mu\mathrm{m}$.255	fixed to smooth cloud
	A_3	Albedo, $3.5\mu\mathrm{m}$.210	fixed to smooth cloud
	E_3	Emissivity mod. factor, $3.5\mu m$	1.66	fixed to smooth cloud
	E_4	Emissivity mod. factor, $4.9\mu m$	1.06	0.0089
	E_5	Emissivity mod. factor, $12\mu m$	1.06	0.00078
	E_6	Emissivity mod. factor, $25\mu m$	1.00	fixed
	E_7	Emissivity mod. factor, $60\mu m$	0.873	0.0042
	E_8	Emissivity mod. factor, $100\mu m$	1.10	7.5×10^{-6}
	E_9	Emissivity mod. factor, $140\mu m$	1.15	-
	E_{10}	Emissivity mod. factor, $240\mu m$	0.858	-

This figure "fig2pg3.jpg" is available in "jpg" format from:

This figure "fig3a.gif" is available in "gif" format from:

This figure "fig3b.gif" is available in "gif" format from:

 ${\bf TABLE~3}$ Comparison of Recent IPD Modelling Prime Parameters

Quantity	Murdock & Price (1985)	Price Wolstencroft		Wheelock et al. (1994)	Jones & Rowan-Robinson (1993)	This Investigation (1998)
Data Base	ZIP	IRAS	IRAS	IRAS	IRAS	DIRBE
Main Cloud Line of Nodes	77 to 110°a	70	79	69	76	77.7
Main Cloud Inclination	1.6 to 3.0 ^a	2.3	1.1	1.73	1.35	2.03
Radial Density Exponent	1.0	1.1	1.3	1.8	1.0	1.34
No. of Bands	0	1°	0	0	2	3
Circumsolar Ring?	N	N	N	N	Y^d	Y
T at 1 AU	$280^{ m b}$	238	255	266	255	286
Temperature Law Exponent	-	0.5	0.5	0.36	0.5	0.467

^aResults insensitive to the value within the range shown.

^bThe effective color temperature.

c Included a "small grain" component which can be considered compensating for the constribution from the asteroidal bands and/or main-belt dust.

^dIncluded a "broad band" component, which could be compensating for the ring and/or main-belt asteroidal dust.

This figure "fig2pg4.jpg" is available in "jpg" format from:

This figure "fig4.gif" is available in "gif" format from:

TABLE 4 ${\rm IPD\ Model\ Component\ Intensities}\ I_{\nu}\ (MJy/sr)\ {\rm at\ Two\ Selected\ Locations\ and\ Times\ (see\ Figure\ 9)}$

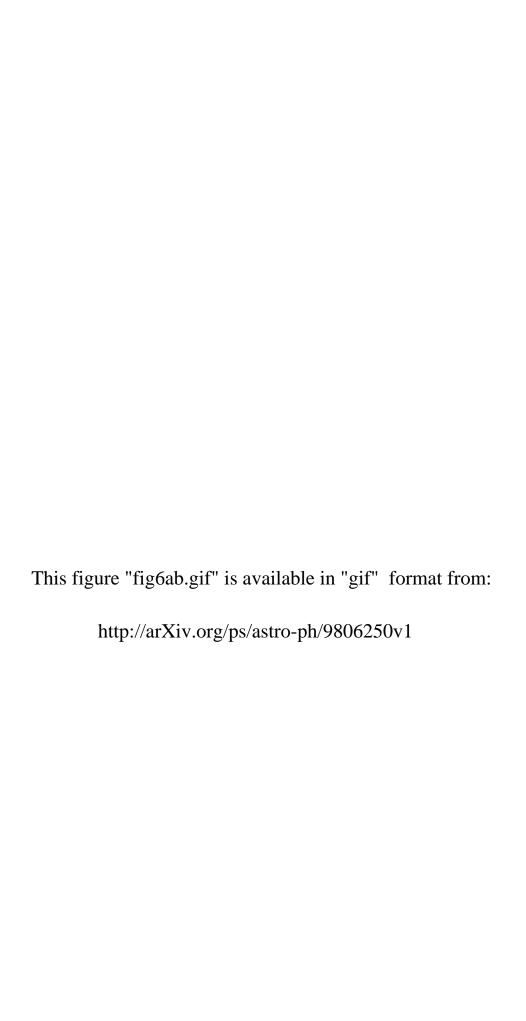
Position	1990	IPD										
(λ, β)	Day	Component	$1.25 \; \mu {\rm m}$	$2.2~\mu\mathrm{m}$	$3.5~\mu\mathrm{m}$	4.9 μm	$12~\mu\mathrm{m}$	$25~\mu\mathrm{m}$	$60~\mu\mathrm{m}$	$100~\mu\mathrm{m}$	$140~\mu\mathrm{m}$	240 μm
$(122^{\circ},0^{\circ})^{\ a}$	109	Smooth Cloud	0.307	0.196	0.133	0.679	28.476	58.063	19.155	6.909	3.346	1.066
		Dust Bands	0.0210	0.0132	0.00837	0.0141	1.938	3.992	2.440	1.232	0.430	0.222
		Ring + Blob	0.0284	0.0189	0.0164	0.109	3.324	5.120	1.618	0.779	0.368	0.122
		Total ZL	0.354	0.229	0.156	0.808	33.875	67.232	23.214	8.993	4.152	1.404
(137°, 46°) b	129	Smooth Cloud	0.144	0.0951	0.0762	0.449	14.669	26.365	7.461	2.572	1.222	0.384
		Dust Bands	0.000854	0.000574	0.000515	0.00114	0.0924	0.146	0.0655	0.0302	0.0101	0.00511
		Ring + Blob	0.00637	0.00426	0.00379	0.0251	0.735	1.118	0.350	0.168	0.0795	0.0241
		Total ZL	0.151	0.0998	0.0807	0.476	15.483	27.619	7.877	2.770	1.312	0.413

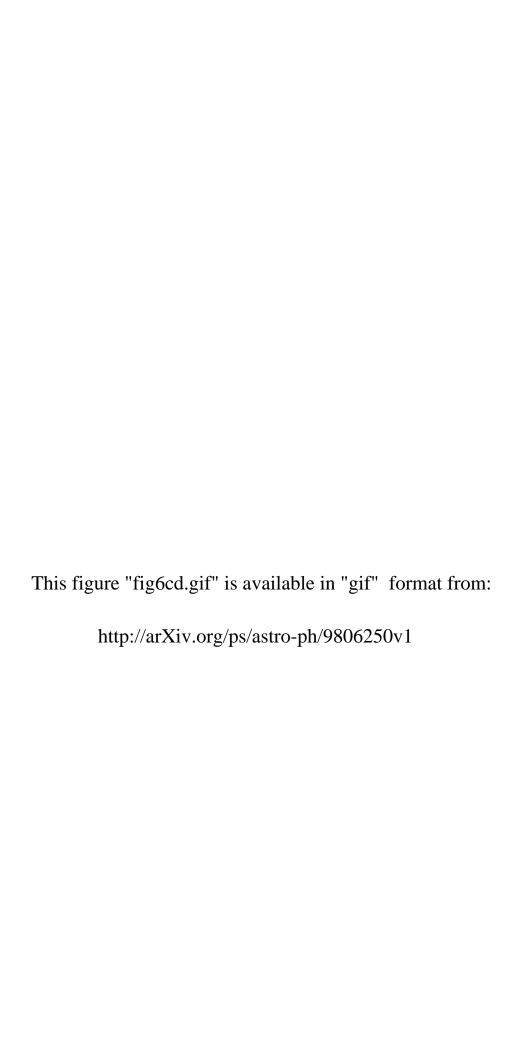
^acorresponds to DIRBE pixel 162811

^bcorresponds to DIRBE pixel 64552

This figure "fig2pg5.jpg" is available in "jpg" format from:

This figure "fig5.gif" is available in "gif" format from:





This figure "fig7.jpg" is available in "jpg" format from:

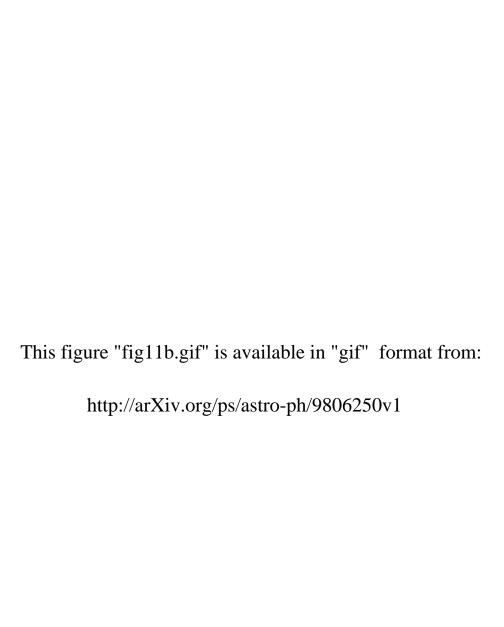
This figure "fig8a.gif" is available in "gif" format from:

This figure "fig8b.gif" is available in "gif" format from: http://arXiv.org/ps/astro-ph/9806250v1

This figure "fig9.gif" is available in "gif" format from:

This figure "fig10.jpg" is available in "jpg" format from:

This figure "fig11a.gif" is available in "gif" format from:



This figure "fig12.gif" is available in "gif" format from:

This figure "fig13.gif" is available in "gif" format from: